

A midpoint projection algorithm for stochastic differential equations on manifolds

Ria Rushin Joseph¹, Jesse van Rhijn^{1,2}, Peter D. Drummond¹

¹*Centre for Quantum Science and Technology Theory,
Swinburne University of Technology, Melbourne, Victoria, Australia and*

²*University of Twente, Enschede, The Netherlands*

Stochastic differential equations projected onto manifolds occur in physics, chemistry, biology, engineering, nanotechnology and optimization, with interdisciplinary applications. Intrinsic coordinate stochastic equations on the manifold are often computationally impractical, and numerical projections are useful in many cases. We show that the Stratonovich interpretation of the stochastic calculus is obtained using adiabatic elimination with a constraint potential. We derive intrinsic stochastic equations for spheroidal and hyperboloidal surfaces for comparison purposes, and review some earlier projection algorithms. In this paper, a combined midpoint projection algorithm is proposed that uses a midpoint projection onto a tangent space, combined with a subsequent normal projection to satisfy the constraints. Numerical examples are given for a range of manifolds, including circular, spheroidal, hyperboloidal, and catenoidal cases, as well as higher-order polynomial constraints and a ten-dimensional hypersphere. We show that in all cases the combined midpoint method has greatly reduced errors compared to methods using a combined Euler projection approach or purely tangential projection. Our technique can handle multiple constraints. This allows manifolds that embody several conserved quantities. The algorithm is accurate, simple and efficient. An order of magnitude error reduction in diffusion distance is typically found compared to the other methods, with reductions of several orders of magnitude in constraint errors.

I. INTRODUCTION

Diffusion processes and stochastic trajectories on curved manifolds inside Cartesian spaces have many applications. The diffusion of atoms or molecules on many types of curved surface occurs in surface physics, biophysics, catalysis, biochemistry, cell biology, and nanotechnology [1–9]. Curved-space diffusion also arises in more abstract problems in general relativity [10], imaginary-time path-integrals [11] and in quantum field theory [12].

Other related problems include systems of stochastic differential equations (SDEs) with conserved quantities [13, 14]. These are used for sampling purposes in studying classical free energies [15], and molecular dynamics. Multidimensional constraints are also found in engineering systems [16, 17], such as in robotics [18–20], where joints may have restricted mobility due to their mechanical design, and experience stochastic forces.

In this paper a hybrid midpoint projection algorithm is introduced for general projected SDEs which combines both tangential and normal projections. A related approach uses an Euler method for each tangential step [21]. Here we generalize this approach to a more accurate midpoint projection algorithm for curved surface stochastic equations.

The resulting algorithm is robust and easily implemented, treating arbitrary drift, diffusion, constraint type and projected manifold dimension. Numerical examples are given, demonstrating excellent error performance both in measures of diffusion distance and in satisfaction of the constraints, which can give rise to large global errors with other methods.

Phase-space stochastic processes [22–24] as well as quantum phase-space methods, for example representations [25, 26] of Majorana physics [27, 28] also lead to

curved space Fokker-Planck [29–31] and stochastic equations [32]. These are some of the many applications of embedded stochastic processes.

Constraint projection occurs in molecular dynamics calculations. For these, specialized techniques are known. Such earlier algorithms are often restricted to these specific problems [33], or are optimized for steady-state distribution sampling, which may not give optimal performance for dynamics [34, 35].

Due to the diversity of the applications, here we develop a general technique applicable to any class of projected stochastic differential equation, including multiplicative noise and arbitrary projections.

Projected diffusion processes can sometimes be treated using stochastic equations for a lower dimensional set of coordinates on the manifold, for example by using spherical polar coordinates on a spherical surface. These can be termed implicit projections: the manifold is implicit in the definition of the coordinates. The embedding theorems [36–38] of Riemannian geometry show that surfaces of arbitrary smooth curvature are equivalent to an appropriate projection. The resulting stochastic equations usually involve multiplicative noise, because the noise coefficients depend on the metric tensor of the manifold. Several numerical algorithms are known for treating such multiplicative stochastic differential equations (SDE)s [39–41].

There are problems with implicit projections [42], especially for closed surfaces. The projected equations may have singularities in the noise and drift terms, due to the analyticity properties of maps [43] and the Poincare-Hopf theorem [44, 45]. Stochastic numerical algorithms may not converge near singularities. Also, the definition of an intrinsic coordinate system [46, 47] on curved surfaces can be a complex problem. There is generally no simple reduced coordinate system for a bi-

ological cell wall or other low-dimensional structures in biology and engineering, due to their complex geometry.

The approach used here is to define a stochastic process in the original coordinates, whose projection satisfies the restrictions of an embedded manifold. This overcomes singularity and variable change issues. Even if the stochastic equation is known on the manifold, it can be useful to employ projections in order to eliminate singularities. The drawback is that discretization can lead to errors from finite step-sizes which may take the stochastic trajectory off the manifold. Such errors may grow rapidly in time as the trajectory moves progressively away from the manifold. These additional global errors are not present in the algorithm proposed here, since the constraints are satisfied with a normal projection after each step.

We first review the theory of manifolds embedded in a Euclidean space. An explanation of how projections can occur physically is obtained through adiabatic elimination with constraint potentials. This is then applied to projections of stochastic processes. The continuous time limit of a constrained stochastic equation is derived as a Stratonovich equation, which is shown to be valid under conditions of finite bandwidth noise and fast projection timescales. Algorithms for multi-dimensional tangential and normal projections are derived. These methods are used to generalize some previous proposals for solving projected stochastic equations.

In order to compare the methods, numerical implementations are carried out. The first examples treat diffusion on circular surfaces, as well as spheroidal and hyperboloidal surfaces in a three-dimensional Cartesian space. We use exact solutions or a semi-implicit intrinsic method using very small time-steps to generate reference results where possible. Simulations using hybrid Euler [21] and tangential methods [48] are also carried out, with errors calculated for measures of distance diffused, and for conservation of constraints. We show that the hybrid midpoint projection algorithm has lower errors in both categories than the other methods.

An outline of the paper is as follows. In Section II, we review the geometric background of manifolds, constraints and projections. In Section III adiabatic elimination is used to justify the interpretation of the projected equation as a Stratonovich equation. Intrinsic stochastic equations are obtained for general spheroidal and one-sheet hyperboloidal surfaces. Section IV gives a discussion of numerical algorithms and the different types of projections. Section V gives numerical examples and error comparisons with either exact or intrinsic diffusion results for circular, catenoidal, spheroidal and hyperboloidal surfaces embedded in Euclidean space. Higher-order polynomial surfaces and hyperspheres are also investigated to model non-quadratic and higher dimensional surfaces. Section VI summarizes the results. In the Appendix we give the intrinsic SDE variables and derivations for spheroidal and hyperboloidal surfaces.

II. MANIFOLDS, CONSTRAINTS AND PROJECTIONS

This paper treats numerical algorithms for projected stochastic equations. We utilize Stratonovich equations [32, 49], which occur in physics as the broad-band limit of a finite bandwidth random process. These follow standard variable change rules. Projections using Ito stochastic calculus [48], are not treated here, and have different properties. While this section reviews standard results, they are useful to define notation.

An unprojected Stratonovich SDE on a Euclidean space \mathbb{R}^n defines a real vector trajectory $\mathbf{x} = [x^1, \dots, x^n]$, where

$$\dot{\mathbf{x}} = \mathbf{a}(\mathbf{x}, t) + \mathbf{B}(\mathbf{x}, t) \boldsymbol{\xi}(t). \quad (2.1)$$

The standard problem is to solve this over a finite interval $[0, T]$, giving a time dependent functional probability density of trajectories $\mathcal{P}([\mathbf{x}(t)])$ conditioned on a specified initial probability distribution $P(\mathbf{x}, t = 0)$. It is usual to focus on the marginal probability densities $P(\mathbf{x}, t)$.

Here $\mathbf{a}(\mathbf{x}, t)$ is a real vector function of \mathbf{x} of dimension n , $\mathbf{B}(\mathbf{x}, t)$ is a real $n \times s$ dimensional matrix function, where we omit the arguments when there is no ambiguity. The real s -dimensional Gaussian noise vector $\boldsymbol{\xi}(t)$ physically has a finite correlation time T_c , and is delta-correlated in the broad-band limit of small T_c , so that:

$$\lim_{T_c \rightarrow 0} \langle \xi^\sigma(t) \xi^\kappa(t') \rangle = \delta^{\sigma\kappa} \delta(t - t'). \quad (2.2)$$

For a small time interval $\Delta t = t_1 - t_0 \gg T_c$, we define a stochastic integral Δw_i as:

$$\Delta w^\sigma = \int_{t_0}^{t_1} \xi^\sigma(t) dt, \quad (2.3)$$

which has the property that

$$\langle \Delta w^\sigma \Delta w^\kappa \rangle = \delta^{\sigma\kappa} \Delta t. \quad (2.4)$$

A single discrete step in the stochastic trajectory is $\Delta \mathbf{x} = \mathbf{x}(t_1) - \mathbf{x}(t_0)$. In the Stratonovich interpretation of stochastic calculus, the midpoint $\bar{\mathbf{x}}$ is the location where the derivatives are evaluated, where

$$\bar{\mathbf{x}} = (\mathbf{x}(t_1) + \mathbf{x}(t_0)) / 2. \quad (2.5)$$

Introducing the corresponding mean time $\bar{t} = (t_1 + t_0) / 2$, the broad-band limit of Eq (2.1) is defined [49] as the limiting behavior of the following implicit stochastic difference equation

$$\Delta \mathbf{x} = \mathbf{a}(\bar{\mathbf{x}}, \bar{t}) \Delta t + \mathbf{B}(\bar{\mathbf{x}}, \bar{t}) \Delta \mathbf{w}. \quad (2.6)$$

In many applications one must project this equation onto a manifold. The broad-band limit is only taken here after adiabatic elimination [50], and we assume that the time-scales of the constraint process are much faster than the noise correlation time, T_c . Although we only

treat real spaces here, these results are applicable to complex spaces, with minor changes. In this section we analyze how such manifolds are obtained, and the corresponding geometrical definitions.

Since we wish to derive algorithms numerically applicable to this problem, we use a coordinate-dependent notation rather than a coordinate-free approach. The results will be expressed in the coordinates of the enclosing (Euclidean) space. In the examples, where possible, explicit comparisons are made to intrinsic coordinate methods.

A. Manifolds

In the section we review the notation that defines the manifold and its properties [51, 52]. We equip \mathbb{R}^n with the Euclidean metric. We use standard contravariant notation for coordinates $\mathbf{x} = \{x^i\}$, and covariant notation for derivatives and normals $\mathbf{n} = \{n_i\}$ to allow the results to be extended to other metrics. Repeated indices will be summed over in the Einstein convention. In the Euclidean case $x^i = x_i$, so the index placement can be ignored.

An m -dimensional sub-manifold is the set of points $\mathbf{y} \in \mathcal{M} \subset \mathbb{R}^n$ for which

$$\mathbf{f}(\mathbf{y}) = 0, \quad (2.7)$$

where \mathbf{f} is a $p = n - m$ dimensional vector constraint function that defines the projection. We assume that the constraint equations are linearly independent. Here $\mathbf{f} = (f^1, \dots, f^p)$ denotes the p constraints.

Local curvature properties are crucial in determining the properties of projected stochastic equations. As a result, it is useful to focus on the classical quadratic geometries. These cover a wide range of Riemann curvatures and topologies. They include positive and negative curvature, and different manifold dimensions and co-dimensions. Locally, most realistic geometries will be comparable to at least one of these cases, and we treat more general cases both in the analytic theory and in the examples.

In the simplest examples below, the constraints are quadratic functions, where f_0^i is a real constant, \mathbf{h}^i is a real vector, \mathbf{G}^i is an $N \times N$ real matrix and:

$$f^i(\mathbf{y}) = f_0^i + \mathbf{h}^i \cdot \mathbf{y} + \mathbf{y}^T \mathbf{G}^i \mathbf{y}. \quad (2.8)$$

This covers circles, parabolas, spheres, hyper-spheres, spheroids, and hyperboloids, as well as intersections of these surfaces when there are multiple constraints. We use these for examples, and choose cases such that $f^0 = -1$ and $\mathbf{h} = 0$ for simplicity. The general algorithms and examples discussed are not limited to these quadratic constraints, but quadratic constraints are useful because these manifolds have well-known intrinsic coordinates and diffusion equations for comparison purposes.

In some cases it is possible to define $\phi \in \mathbb{R}^m$ as a new intrinsic coordinate system for the set of points restricted to the manifold. For example, on the surface of

a sphere one may use polar coordinates. In such cases, a vector mapping function Φ exists where $\phi = \Phi(\mathbf{y})$ for every Euclidean coordinate \mathbf{y} in the original manifold \mathcal{M} .

Even if they exist, such mapping functions lead to singularities for a compact manifold, and may not be able to be expressed in a closed form. As a result, we use algorithms that can be expressed in the original Euclidean coordinates. Intrinsic coordinates are used for numerical examples, although such comparisons are only available in special cases where analytic transforms exist.

B. Tangent and normal spaces

In many cases it is not convenient or practical to use intrinsic coordinates, and it is necessary to integrate in the original Euclidean frame of reference. This requires a knowledge of the tangential and normal spaces. Near to a point \mathbf{y} in the manifold, from a Taylor expansion of the j -th constraint equation,

$$f^j(\mathbf{x}) = \sum_{i=1}^n \Delta^i f_{,i}^j(\mathbf{y}) + O(|\Delta|^2), \quad (2.9)$$

where $\Delta^i = x^i - y^i$, $\partial_i \equiv \partial/\partial x^i$, and the constraint derivative is

$$f_{,i}^j \equiv \partial_i f^j. \quad (2.10)$$

From this condition, $v_{\perp i}^j = \partial_i f^j$ is called the j -th normal vector, \mathbf{v}_{\perp}^j , where the lower index indicates a covariant vector, and the upper index labels the constraint, f^j , so that $j = 1, \dots, p$. Any orthogonal vector \mathbf{v}^{\parallel} such that $\mathbf{v}^{\parallel} \cdot \mathbf{v}_{\perp}^j = 0$ locally satisfies the j -th constraint, although it may not satisfy the other constraints. In general the normal vectors \mathbf{v}_{\perp}^j may not be orthogonal to each other. They are assumed to be linearly independent at all locations in order to generate a differentiable manifold locally isomorphic to \mathbb{R}^m without a singular point [51]. Singular points may occur with some choices of multiple projections, but these are unphysical and can lead to convergence issues.

One can use the gradient vectors of the constraints to define a set of orthonormal vectors \mathbf{n}^j that span the p -dimensional space of vectors normal to each constraint. This requires orthogonalization of the set \mathbf{v}_{\perp}^j , either by Gram-Schmidt or other methods [53]. As a result, the orthonormal vectors \mathbf{n}^j have the property that, for $i, j = 1, \dots, p$:

$$\begin{aligned} \mathbf{n}^j \cdot \mathbf{v}_{\perp}^j &\neq 0 \\ \mathbf{n}^i \cdot \mathbf{n}^j &= \delta^{ij}. \end{aligned} \quad (2.11)$$

Similarly, there is a set of orthonormal tangent vectors \mathbf{m}_i , where $i = 1, \dots, m$. These define the tangent space of the manifold, and give an orthonormal basis of m

contravariant vectors orthogonal to *all* of the normal vectors \mathbf{v}_\perp^j , so that, for $j = 1, \dots, p$ and $i = 1, \dots, m$:

$$\begin{aligned} \mathbf{m}_i \cdot \mathbf{n}^j &= \mathbf{m}_i \cdot \mathbf{v}_\perp^j = 0 \\ \mathbf{m}_i \cdot \mathbf{m}_j &= \delta_{ij}. \end{aligned} \quad (2.12)$$

One can define a vector space consisting of all vectors tangent to \mathcal{M} at any point $\mathbf{y} \in \mathcal{M}$. This is the tangent space, $T_y\mathcal{M}$, and it is spanned by the basis \mathbf{m}_j for $j = 1, \dots, m$. The orthogonal complement to the tangent space is the normal space, spanned by the basis \mathbf{n}^j for $j = 1, \dots, p$.

For every vector $\mathbf{v} \in \mathbb{R}^N$ and manifold coordinate $\mathbf{y} \in \mathbb{R}^m$, a vector decomposition can therefore be written as follows [54]:

$$\mathbf{v} = \mathbf{v}_\parallel + \mathbf{v}_\perp, \quad \mathbf{v}_\parallel \in T_x\mathcal{M}, \quad \mathbf{v}_\perp \in T_x^\perp\mathcal{M}, \quad (2.13)$$

provided \mathbf{v}_\parallel , \mathbf{v}_\perp are the tangential and normal projection of $\mathbf{v} \in \mathbb{R}^m$ respectively and $T_y^\perp\mathcal{M}$ is the orthogonal complement of $T_y\mathcal{M}$. If we consider the sphere, the vectors \mathbf{v}_\parallel perpendicular to the radii are tangents at \mathbf{y} with a basis \mathbf{m}_i , while the radial vectors \mathbf{v}_\perp are the normals, with a basis \mathbf{n}^j .

This can be expressed in terms of projection operators \mathcal{P}^\perp and $\mathcal{P}_\mathbf{y}^\parallel$. These satisfy the fundamental property of mathematical projections on sets that, once projected, a coordinate doesn't change under further projections, so $\mathcal{P}(\mathcal{P}(\mathbf{x})) = \mathcal{P}(\mathbf{x})$.

C. Tangential projections

Eq. (2.12) guarantees that any tangent vector of form $\mathbf{y} + \epsilon\mathbf{m}_i$ is in the tangent space. In a neighborhood of a point $\mathbf{y} \in \mathcal{M}$, all constraints are satisfied up to terms of order ϵ^2 since for tangent vectors \mathbf{m}_i and a small coefficient ϵ :

$$f^j(\mathbf{y} + \epsilon\mathbf{m}_i) = \epsilon\mathbf{m}_i \cdot \mathbf{v}_\perp^j + O(\epsilon^2) \approx 0. \quad (2.14)$$

A general tangential projection of any time-evolution equation is obtained by projecting an arbitrary derivative vector $\boldsymbol{\delta}$ at each location onto the tangent space of the manifold. This type of projection depends on the location, so we use the notation of $\boldsymbol{\delta}^\parallel = \Pi_\mathbf{y}^\parallel(\boldsymbol{\delta})$, for a tangential projection of a derivative vector $\boldsymbol{\delta}$ at a point on or near the manifold.

One can obtain the tangential projection $\boldsymbol{\delta}^\parallel$ in a simple case of a one-dimensional constraint, by removing the normal component from the vector $\boldsymbol{\delta}$ using Eq. (2.13), so that:

$$\begin{aligned} \boldsymbol{\delta}^\parallel &= \boldsymbol{\delta} - (\boldsymbol{\delta} \cdot \mathbf{v}_\perp) \mathbf{v}_\perp / |\mathbf{v}_\perp|^2, \\ &\equiv (\mathbf{I} - \mathbf{n} \otimes \mathbf{n}) \boldsymbol{\delta}. \end{aligned} \quad (2.15)$$

Here $\mathbf{n} \otimes \mathbf{n}$ is an outer vector product defined as the matrix $[\mathbf{n} \otimes \mathbf{n}]_{ij} = n_i n_j$, \mathbf{n} is the normal vector at \mathbf{y} , \mathbf{I} is the identity matrix, and $(\mathbf{I} - \mathbf{n} \otimes \mathbf{n})$ is called the tangential operator [55].

More generally, for multiple constraints, the projection must remove multiple normal components \mathbf{n}^j , so one must define:

$$\begin{aligned} \boldsymbol{\delta}^\parallel &= \mathcal{P}_\mathbf{y}^\parallel(\boldsymbol{\delta}) \\ &= \left(\mathbf{I} - \sum_{j=1}^p \mathbf{n}^j \otimes \mathbf{n}^j \right) \boldsymbol{\delta}. \end{aligned} \quad (2.16)$$

D. Normal projections

In a normal projection, points in a neighborhood of \mathcal{M} are projected onto the nearest point on \mathcal{M} . The projection $\mathbf{y} = \mathcal{P}^\perp(\mathbf{x})$ therefore takes an initial $\mathbf{x} \in \mathbb{R}^n$, and maps it onto the nearest manifold coordinate \mathbf{y} .

For example, in the spherical case, a path in Euclidean coordinates \mathbf{x} in n -space is projected onto the $n - 1$ dimensional hyper-spherical surface of a ball of radius r around the origin, at every step on the path. An exact projection function in this case is:

$$\mathbf{y} = \mathcal{P}^\perp(\mathbf{x}) = \frac{r\mathbf{x}}{|\mathbf{x}|}, \quad (2.17)$$

which is defined for all $\mathbf{x} \neq 0$. Exact normal projections are only obtainable in special cases. Hence, we now consider approximate normal projections valid near a manifold point.

To obtain the general approach which solves this, we introduce a Lagrange multiplier vector \mathbf{c} . Given an initial point \mathbf{x} and a projected point \mathbf{y} on the manifold, one must find Lagrange multipliers $c_j(\mathbf{x}, \mathbf{y})$ such that:

$$\begin{aligned} \mathbf{y} &= \mathbf{x} + \sum_{j=1}^p c_j(\mathbf{x}, \mathbf{y}) \mathbf{n}^j(\mathbf{y}), \\ f^j(\mathbf{y}) &= 0. \end{aligned} \quad (2.18)$$

Solving for \mathbf{y} corresponds to minimizing the functional $k(\mathbf{y}) = |\mathbf{y} - \mathbf{x}|^2$, subject to the constraint that $f^i(\mathbf{y}) = 0$. This is generally a hard computational problem, but can be solved approximately with a Taylor expansion, valid if $|\mathbf{y} - \mathbf{x}|$ is small. Since $f^j(\mathbf{y}) = 0$, therefore to first order in a Taylor series about \mathbf{y} , one finds that

$$f^j(\mathbf{x}) = (\mathbf{x} - \mathbf{y}) \cdot \mathbf{v}_\perp^j(\mathbf{y}) + O(\mathbf{x} - \mathbf{y})^2. \quad (2.19)$$

This follows since the \mathbf{v}_\perp^j vectors are all derivatives. From Eq (2.18),

$$\mathbf{y} - \mathbf{x} = \sum_{j=1}^p c_j(\mathbf{x}, \mathbf{y}) \mathbf{n}^j(\mathbf{y}). \quad (2.20)$$

One must therefore solve the following nonlinear implicit equation:

$$f^i(\mathbf{x}) = - \sum_{j=1}^p M^{ij}(\mathbf{y}) c_j(\mathbf{x}, \mathbf{y}) + O(\mathbf{x} - \mathbf{y})^2. \quad (2.21)$$

In this equation, the normal projection matrix \mathbf{M} is defined so that its components are the the inner products of $\mathbf{v}_\perp^i(\mathbf{y})$ with the normal vectors $\mathbf{n}^j(\mathbf{y})$, i.e.,

$$M^{ij}(\mathbf{y}) = \mathbf{v}_\perp^i(\mathbf{y}) \cdot \mathbf{n}^j(\mathbf{y}). \quad (2.22)$$

Solving for c_j , one obtains an implicit equation:

$$c_i(\mathbf{x}, \mathbf{y}) = - \sum_{j=1}^p [\mathbf{M}(\mathbf{y})]_{ij}^{-1} f^j(\mathbf{x}). \quad (2.23)$$

Given an initial estimate \mathbf{x} , a normal projection is obtained by solving Eq. (2.23) for \mathbf{c} , and hence obtaining \mathbf{y} using iteration, where the matrix $\mathbf{M}(\mathbf{x})$ is used instead of $\mathbf{M}(\mathbf{y})$ to lowest order. In the algorithms described here, a single iterative step is used because the trajectories are already close to the manifold, so that:

$$\mathbf{y} = \mathcal{P}^\perp(\mathbf{x}) \approx \mathbf{x} - \sum_{i,j=1}^p \mathbf{n}^i(\mathbf{x}) [\mathbf{M}(\mathbf{x})]_{ij}^{-1} f^j(\mathbf{x}). \quad (2.24)$$

In the case of a one-dimensional constraint, since $|\mathbf{n}^\perp(\mathbf{x})| = 1$, it follows that $\mathbf{v}^\perp(\mathbf{x}) \cdot \mathbf{n}(\mathbf{x}) = |\mathbf{v}^\perp(\mathbf{x})|$. For small $|\mathbf{y} - \mathbf{x}|$, one therefore obtains:

$$\mathbf{y} \approx \mathbf{x} - \mathbf{v}^\perp(\mathbf{y}) |\mathbf{v}^\perp(\mathbf{x})|^{-2} f(\mathbf{x}). \quad (2.25)$$

III. ADIABATIC ELIMINATION FOR PROJECTED EQUATIONS

To understand the origin of projections of a stochastic equation, one must ask: what physical or mathematical process restricts the path to a manifold? Here, we treat a constraining potential, as a common situation found in physics, and also used for quantum applications where there are similar issues [52]. While this is not universally applicable for all projected stochastic equations, it explains our choice of stochastic calculus.

We introduce a local mapping function Φ inside a local patch where $\phi^\parallel = \Phi(\mathbf{y})$ for Euclidean coordinates \mathbf{y} in the original manifold \mathcal{M} . For purposes of adiabatic elimination, we extended this locally to an invertible mapping $\mathbf{x} = \mathbf{x}(\phi)$ including nearby off-manifold points, with a complete set of coordinates $\phi = [\phi^\parallel, \phi^\perp]$ such that $f^j(\mathbf{x}(\phi)) = 0$ if $\phi^\perp = 0$.

Specifically, we define ϕ^\perp to correspond to points in the normal space, where if \mathbf{y} is a manifold point, then for nearby points \mathbf{x} in Euclidean space, ϕ^\perp is the distance along a normal vector:

$$\phi^{\perp,i}(\mathbf{x}) = (\mathbf{x} - \mathbf{y}) \cdot \mathbf{n}^{i\perp}(\mathbf{y}). \quad (3.1)$$

To return to the spherical example, the coordinate ϕ^\perp for overall dimension $n = 3$ is the radial coordinate in that case.

A. Constraining potentials

Constraining potentials are essential for constraining particles on a manifold, and provide a model for the origin of a projected stochastic equation. We assume that the constraint conditions originate in a scalar constraint potential

$$u(\mathbf{x}) = \frac{\lambda}{2} \sum_{j=1}^p [f^j(\mathbf{x})]^2. \quad (3.2)$$

The projected stochastic equation is the adiabatic limit for $\lambda \rightarrow \infty$, of a continuous stochastic process in which the initial SDE in Eq. (2.1) includes the constraint as a potential, so that:

$$\dot{x}^i = a^i(\mathbf{x}, t) - \partial^i u(\mathbf{x}) + \sum_k B_\sigma^i(\mathbf{x}, t) \xi^\sigma. \quad (3.3)$$

Here $\partial^i u \equiv [\nabla u]^i$ is the contravariant derivative, which equals the covariant derivative $\partial_i u$ for our metric choice. The drift for motion including the confining potential is then $\mathbf{a}_\lambda(\mathbf{x}) = \mathbf{a} - \nabla u(\mathbf{x})$. The gradient of the potential is,

$$\nabla u(\mathbf{x}) = \lambda \sum_j \mathbf{v}_\perp^j(\mathbf{y}) f^j(\mathbf{x}). \quad (3.4)$$

In terms of the local coordinates ϕ , the constrained equation is:

$$\dot{\phi} = \mathbf{J} [\mathbf{a}_\lambda + \mathbf{B}\xi]. \quad (3.5)$$

where the Jacobian \mathbf{J} is defined as:

$$J_j^i = \frac{\partial \phi^i}{\partial x^j}. \quad (3.6)$$

From the definition of the normal coordinates in Eq (3.1), this implies that for $i > m$, where m is the manifold dimension, and $\mathbf{x} \approx \mathbf{y}$, the Jacobian is equal to the corresponding normal vector:

$$J_j^i = \mathbf{n}_j^i(\mathbf{y}). \quad (3.7)$$

The reduction of the number of independent degrees of freedom that result from a minimization of the potential u is equivalent to adiabatic elimination of the fast transverse variables in a stochastic equation, treated next.

B. Adiabatic elimination

Adiabatic elimination will be used in order to analyze how projections are applied to stochastic equations. As has been recently pointed out [48], there can be ambiguity in defining the which type of stochastic equation is obtained after projection. This depends on how the

projection occurs. We assume that the original SDE in Eq. (2.1) has noise with a finite bandwidth. Hence, it follows the Stratonovich calculus in the broad-band limit [49].

The projection is assumed to occur through an adiabatic elimination process, due to the constraint potential. The resulting diffusion or noise is generally state-dependent, even if not originally. To analyze this, we follow a similar method to the work of Gardiner [50]. In general, a direct approach to adiabatic elimination is obtained through dividing up the variables into a “fast” and “slow” set. In the present context, these are locally in the direction of the normal and tangential coordinates.

We take a given point $\bar{\phi}$ on the manifold such that $f(\mathbf{x}(\bar{\phi})) = 0$. We now consider a trajectory $\phi(t)$ near $\bar{\phi}$, governed by the constrained stochastic equation in Eq. (3.5), so that

$$\Delta(t) \equiv \phi(t) - \bar{\phi}. \quad (3.8)$$

Changes in the coordinate, Δ , are divided into “slow” coordinates Δ^{\parallel} for motion inside the manifold, and “fast” or normal coordinates Δ^{\perp} for motion outside the manifold. For a small displacement we obtain:

$$\Delta(t) = \sum_{i=1}^m \Delta_i^{\parallel}(t) + \sum_{j=1}^p \Delta_j^{\perp}(t). \quad (3.9)$$

In a neighborhood of the manifold where $\mathbf{x} \approx \mathbf{y}$, these have equations given by the chain rule for variable changes, noting that we only consider smooth differentiable functions here:

$$\dot{\Delta} = \mathbf{J}(\bar{\phi} + \Delta) [\mathbf{a}_{\lambda}(\mathbf{x}(\bar{\phi} + \Delta)) + \mathbf{B}(\mathbf{x}(\bar{\phi} + \Delta)) \boldsymbol{\xi}]. \quad (3.10)$$

1. Fast variables

Expanding the displacement Δ according to Eq. (3.9), we define

$$\begin{aligned} a_{\perp}^i &= \mathbf{n}^i \cdot \mathbf{a} \\ \mathbf{b}_{\perp}^i &= \mathbf{n}^i \cdot \mathbf{B} \end{aligned} \quad (3.11)$$

Here a_{\perp}^i is the i -th component of the normal drift, and the inner-product notation refers to inner products in the original Euclidean space. Each term \mathbf{b}_{\perp}^i is a covariant vector in the s -dimensional space of noise terms:

$$b_{\perp\sigma}^i = \sum_{j=1}^n n_j^i B_{\sigma}^j. \quad (3.12)$$

This gives a locally valid stochastic equation for the fast variables, where the inner product $\mathbf{b}_{\perp}^i \cdot \boldsymbol{\xi} = \sum_{\sigma} b_{\perp\sigma}^i \xi^{\sigma}$ is in the noise-vector space:

$$\dot{\Delta}_{\perp}^i = a_{\perp}^i - \lambda \sum_{k=1}^p R^{ik} \Delta_{\perp}^k + \mathbf{b}_{\perp}^i \cdot \boldsymbol{\xi}. \quad (3.13)$$

Here we define the constraint linear response matrix \mathbf{R} as

$$R^{ik} = \sum_{j=1}^p \left(\mathbf{v}_{\perp}^j \cdot \mathbf{n}^i \right) \left(\mathbf{v}_{\perp}^j \cdot \mathbf{n}^k \right). \quad (3.14)$$

One can rewrite \mathbf{R} in a factored form as $\mathbf{R} = \mathbf{M}^T \mathbf{M}$, where $M^{ij} = \mathbf{v}_{\perp}^i \cdot \mathbf{n}^j$ is the normal projection matrix of (2.22). From Eq (2.11), the diagonal elements of \mathbf{R} are non-vanishing. As a result, \mathbf{R} is a symmetric, positive definite matrix, provided the constraints are non-singular. Since it must have positive eigenvalues, the adiabatic limit is found by taking the limit of $\lambda \rightarrow \infty$. This is equivalent to setting $\dot{\Delta}_{\perp}^i = 0$, due to the rapid equilibration that occurs.

We also assume that $\lambda T_c \gg 0$, with the result that the “fast” set Δ^{\perp} experience a large rate of change defined by λ , and relaxes to equilibrium on a short time scale of $1/\lambda$. Therefore, in the adiabatic limit, $\Delta^{\perp} = 0$, and the system is constrained to the tangent space.

2. Slow variables

By contrast, the slow set Δ^{\parallel} does not relax at the same rate. The constraint terms vanish, since the Jacobian for these variables is orthogonal to the constraint terms. Substituting the resulting values into the “slow” equations therefore leads to a simpler projected equation with fewer independent variables. We define, for $\mu = 1, \dots, m$:

$$\dot{\Delta}^{\mu} = \sum_j J_j^{\mu} (a^j + B_{\sigma}^j \xi^{\sigma}) \quad (3.15)$$

This equation can be written as an equation purely in terms of the intrinsic manifold coordinates, as:

$$\dot{\Delta}^{\mu} = \alpha^{\mu} + \beta_{\sigma}^{\mu} \xi^{\sigma} \quad (3.16)$$

with the definitions that:

$$\begin{aligned} \alpha^{\mu} &= \sum_j J_j^{\mu} a^j \\ \beta_{\sigma}^{\mu} &= \sum_j J_j^{\mu} B_{\sigma}^j. \end{aligned} \quad (3.17)$$

This leads to an important question. Is the projected SDE an Ito or Stratonovich equation?

We assume that the original equation prior to projection has a finite bandwidth. This means that ordinary calculus rules are applicable at each stage. The broad-band limit is then taken after adiabatic elimination, subject to the restriction that $\lambda T_c \gg 0$, which leads to a Stratonovich interpretation.

Defining $\mathbf{a}_{\parallel}(\mathbf{x}) = \mathcal{P}_{\mathbf{x}}^{\parallel}(\mathbf{a}(\mathbf{x}))$ and $\mathbf{B}_{\parallel}(\mathbf{x}) = \mathcal{P}_{\mathbf{x}}^{\parallel}(\mathbf{B}(\mathbf{x}))$, the resulting Stratonovich equation can also be rewritten in a shorthand form as:

$$\dot{\mathbf{x}} = \mathbf{a}_{\parallel}(\mathbf{x}) + \mathbf{B}_{\parallel}(\mathbf{x}) \boldsymbol{\xi}(t). \quad (3.18)$$

Gardiner [50] demonstrates that in two-dimensional cases, then even if the original equation is in the broad-band limit, adiabatic elimination will lead to the Stratonovich interpretation of the resulting SDE, if there are no fast variables in the noise coefficients. More generally, one should make a case-by-case analysis to determine if there are additional stochastic correction terms. The constraint equations are now automatically satisfied, provided they are satisfied initially, since

$$\dot{f}^i = \dot{\mathbf{x}} \cdot \nabla f^i = 0. \quad (3.19)$$

While these equations are correct in the continuous limit, it is important to take measures to ensure the solutions remain on the manifold for a finite time-step. To explain this, if we use the midpoint definition of Eq. (2.5), the discrete midpoint algorithm in Cartesian coordinates can be written as:

$$\Delta \mathbf{x} = \mathbf{a}^{\parallel}(\bar{\mathbf{x}}, \bar{t}) \Delta t + \mathbf{B}^{\parallel}(\bar{\mathbf{x}}, \bar{t}) \Delta \mathbf{w}. \quad (3.20)$$

Due to discretization error, the path may not remain on the manifold with this method, as we show in numerical examples below. Since our derivation requires that the constraints are satisfied exactly, we will show that it is better to make an additional normal projection to satisfy the constraints, so that the final algorithm reads:

$$\Delta \mathbf{x} = \mathcal{P}^{\perp} \left\{ \mathbf{x} + \mathbf{a}^{\parallel}(\bar{\mathbf{x}}, \bar{t}) \Delta t + \mathbf{B}^{\parallel}(\bar{\mathbf{x}}, \bar{t}) \Delta \mathbf{w} \right\} - \mathbf{x}. \quad (3.21)$$

C. Intrinsic stochastic equations

To summarize the preceding results, the projected coordinates $\mathbf{y} = \mathcal{P}(\mathbf{x})$ are coordinates on an embedded manifold in Euclidean space \mathbb{R}^n . A further transformation can be made to obtain intrinsic coordinates on the manifold with lower dimensionality. Hence, to obtain ϕ , we define

$$\phi = \Phi(\mathbf{y}). \quad (3.22)$$

One can make subsequent transformations on ϕ to obtain other systems of coordinates on the manifold, such as defining spherical polar coordinates with rotated polar directions, but these are all isomorphic to the set of projected coordinates $\{\mathcal{P}(\mathbf{x})\}$.

The diffusion and drift in (3.18) is in a Stratonovich form [32], appropriate for many physical problems. This is the wide-band limit of a physical noise, and is valid in most cases of adiabatic elimination. As a result, one can use ordinary calculus rules to transform this into an intrinsic n -dimensional stochastic differential equation (SDE):

$$\dot{\phi} = \alpha(\phi) + \beta(\phi) \xi, \quad (3.23)$$

where $\alpha(\phi)$, $\beta(\phi)$ are given by (3.17). The s -dimensional noise vector ξ is Gaussian and delta-correlated, and follows Eq. (2.2).

The corresponding diffusion or Fokker-Planck equation (FPE) [30, 56] is for a probability density $P(\phi, t)$ in an n -dimensional real vector space or manifold \mathcal{M} , where the intrinsic coordinates are ϕ . Our notation treats intrinsic phase-space coordinates as contravariant vectors ϕ^{μ} , and derivatives as covariant quantities $\partial_{\mu} \equiv \partial/\partial\phi^{\mu}$. This leads to an FPE of form:

$$\frac{\partial P}{\partial t} = \left[-\partial_{\mu} \alpha^{\mu}(\phi) + \frac{1}{2} \partial_{\mu} \beta_{\sigma}^{\mu}(\phi) \partial_{\nu} \beta_{\sigma}^{\nu}(\phi) \right] P, \quad (3.24)$$

where we use the Einstein summation convention for repeated indices $\mu = 1, \dots, n$, $\sigma = 1, \dots, s$, and the corresponding diffusion matrix can also be regarded as a contravariant metric tensor [30]. To avoid confusion with the induced metric defined below, we use the notation of a diffusion matrix $D^{\mu\nu}$,

$$D^{\mu\nu}(\phi) = \sum_{\sigma} \beta_{\sigma}^{\mu}(\phi) \beta_{\sigma}^{\nu}(\phi). \quad (3.25)$$

Growth restrictions on coefficients [57] are needed to guarantee that solutions exist.

D. Ito and covariant diffusion

For comparison with previous work, there are several types of drift term for stochastic equations, corresponding to other forms of differential terms in the FPE and different types of stochastic calculus. The Stratonovich drift α used here is related to the Ito drift α_I [32, 49], found in Ito stochastic equations, by the mapping:

$$\alpha_I^{\mu} = \alpha^{\mu} + \frac{1}{2} \sum_{\sigma} \beta_{\sigma}^{\nu} \partial_{\nu} \beta_{\sigma}^{\mu}. \quad (3.26)$$

In the numerical examples, we take the simplest case that the original manifold has a locally Euclidean metric and Euclidean diffusion $g_{ij}^E = \delta_{ij}$ on a tangent plane, although this is not the most general case. The mapping to intrinsic coordinates defines an induced metric g , which is in general a curved metric [38], such that:

$$g_{\mu\nu} = \frac{\partial y^i}{\partial \phi^{\mu}} \frac{\partial y^j}{\partial \phi^{\nu}} \delta_{ij}. \quad (3.27)$$

We therefore consider an m -dimensional manifold equipped with a metric $g_{\mu\nu}$, in an intrinsic coordinate system with coordinates ϕ . As an example, the usual Fokker-Planck equation governing non-driven Euclidean diffusion on this manifold is given by

$$\frac{\partial \tilde{P}}{\partial t} = \frac{1}{2} D \tilde{\Delta} \tilde{P}, \quad (3.28)$$

where $\tilde{\Delta} = \nabla_{\mu} \nabla^{\mu}$ is the Laplace-Beltrami operator, \tilde{P} is the covariant probability density, and D is the covariant

diffusion coefficient. This FPE is in a covariant form, meaning that probability is conserved with respect to the measure $\sqrt{g}d^m\phi$, where $g = \det(g_{\mu\nu})$. If one scales the covariant probability density by \sqrt{g} , the result is a probability density P that is conserved with respect to $d^m\phi$.

Inserting also the formula [56, 58],

$$\tilde{\Delta}\tilde{P} = \frac{1}{\sqrt{g}}\partial_\mu(\sqrt{g}\partial^\mu\tilde{P}), \quad (3.29)$$

one finds that

$$\frac{\partial P}{\partial t} = \frac{D}{2}\partial_\mu\left(\sqrt{g}g^{\mu\nu}\partial_\nu\frac{P}{\sqrt{g}}\right), \quad (3.30)$$

with $g^{\mu\nu} = [g_{\mu\nu}]^{-1}$, and $P = \sqrt{g}\tilde{P}$. Equivalently, using Einstein summation convention for repeated indices, one obtains the self-adjoint diffusion equation,

$$\frac{\partial P}{\partial t} = -D\partial_\mu\left(\frac{1}{4}g^{\mu\nu}\partial_\nu\ln g\right)P + \frac{D}{2}\partial_\mu g^{\mu\nu}\partial_\nu P. \quad (3.31)$$

In this expression the self-adjoint drift is

$$\alpha_a^\mu = \frac{D}{4}g^{\mu\nu}\partial_\nu\ln g. \quad (3.32)$$

This FPE may be transformed to the Stratonovich form, from which one easily reads off an equivalent system of SDEs by introducing $Dg^{\mu\nu} = \sum_\sigma\beta_\sigma^\mu\beta_\sigma^\nu$, and defining

$$\alpha^\mu = \alpha_a^\mu + \frac{1}{2}\sum_\sigma\beta_\sigma^\mu\partial_\nu\beta_\sigma^\nu, \quad (3.33)$$

The corresponding projected Stratonovich SDE is then

$$\dot{\phi}^\mu = \alpha^\mu + \beta_\sigma^\mu\xi^\sigma. \quad (3.34)$$

However, the fact that the final diffusion matrix is proportional to the induced metric is due to the form of the initial diffusion matrix, which was chosen equal to the Euclidean metric tensor for this example. This is not always the case, and the final diffusion matrix has to be worked out accordingly.

E. Hypersphere

As an illustration, consider a hyper-spherical manifold with $|\mathbf{x}|^2 = 1$ and isotropic diffusion with $\mathbf{B} = \mathbf{I}$ in the original Euclidean space. Writing Eq. (2.1) as a difference equation as in Eq. (2.6) leads to

$$\Delta\mathbf{x} = \Delta\mathbf{w}. \quad (3.35)$$

where the Gaussian noise $\Delta\mathbf{w}$ integrated over an interval Δt is correlated according to Eq. (2.4).

Simply projecting this according to the constraint naively leads to a projected equation:

$$\Delta\mathbf{x} = \mathcal{P}^\perp(\mathbf{x} + \Delta\mathbf{w}) - \mathbf{x}, \quad (3.36)$$

where $\mathcal{P}^\perp(\mathbf{x})$ projects the new vector $\mathbf{y} = \mathbf{x} + \delta$ normally onto the sphere, or more generally onto a manifold \mathcal{M} . Instead of this approach, using the adiabatic elimination combined with a potential, one might choose that:

$$u(\mathbf{x}) = \frac{\lambda}{2}\left(|\mathbf{x}|^2 - 1\right)^2. \quad (3.37)$$

On the projected manifold, the restoring drift towards the surface is normal, since:

$$\nabla u(\mathbf{y}) = 2\lambda\mathbf{y}\left(|\mathbf{y}|^2 - 1\right). \quad (3.38)$$

For a tangential projection $\mathcal{P}_\mathbf{x}^\parallel$ on the manifold, the resulting stochastic equation is then:

$$\dot{\mathbf{x}} = \mathcal{P}_\mathbf{x}^\parallel\boldsymbol{\xi} = \boldsymbol{\xi}_\mathbf{x}^\parallel. \quad (3.39)$$

From the results above, this is a Stratonovich equation [49]. The corresponding intrinsic equations for the 3-dimensional case (see Appendix) have an unphysical singularity at the poles, which is eliminated using projections:

$$\begin{aligned} \dot{\theta} &= \frac{1}{2}\cot\theta + \xi^\theta \\ \dot{\phi} &= \frac{\xi^\phi}{\sin\theta}. \end{aligned} \quad (3.40)$$

IV. STOCHASTIC PROJECTION ALGORITHMS

We first summarize the numerical algorithms for tangential and normal projections, and then explain how these are used in projected stochastic equations. In some cases [48], a tangential projection of the coefficients of a Stratonovich SDE is used. However, this doesn't guarantee the solution is on the manifold. The difficulty with tangential methods is that global errors can accumulate at finite step-size. Hence, the final result can move arbitrarily far way from the desired manifold. Other proposed methods that use restrictions to a manifold are often limited to two-dimensional surfaces in three-dimensional spaces [59].

Another approach commonly applied to physics problems [21], is to employ a tangentially projected Ito-Euler step followed by normal projections to remain on the manifold. Similar techniques are used in molecular dynamics applications to compute free energies [15, 34].

Compared to a purely tangential approach, this has the advantage that the final normal projection keeps the solution on the manifold. However, Ito stochastic equations are not always equivalent to Stratonovich stochastic equations, unless appropriate corrections are employed.

The hybrid approach described here is to use a stochastic method of known convergence properties to solve the tangentially projected Stratonovich equations, (3.18), followed by normal projection to the manifold after each step. This combines the best features of both the tangential and normal projection approaches. There are also stochastic methods of higher orders available [40]. We refer the reader to recent work in this area [35].

Our approach is illustrated with a hybrid midpoint projection algorithm that combines a midpoint method [39] instead of an Euler step, together with normal projection. The manifold is given by the constraint equations $f^i(\mathbf{x}) = 0$, where \mathbf{x} is defined as a midpoint for each tangential step. We assume the existence of an orthogonalization algorithm that generates an orthonormal set of vectors, $S^\perp = \{\mathbf{n}^1, \dots, \mathbf{n}^p\}$, from a set of gradient vectors $S = \{\mathbf{v}_\perp^1, \dots, \mathbf{v}_\perp^p\}$, using one of the known standard techniques [53, 60].

The three algorithms compared here all use the notation that $\mathbf{x}_0, \mathbf{x}_1$ are the initial and final locations of a step in time, Δt is the step-size, and $\Delta \mathbf{w}$ are random Gaussian variables. They have correlations that correspond to a discretized delta-function in time, as described in Eq (2.4).

In the next section, we give examples of the use of these algorithms by comparing them either with exact results or with well-converged, high-accuracy simulations, for a wide range of dimensions and different constraint types, namely:

- Kubo oscillators
- catenoids
- hyperspheres
- spheroids
- hyperboloids
- polynomial surfaces

A. Error properties

There are three main errors when solving projected stochastic equations numerically. The first is caused by the finite sample number, N_s . This means that probabilities or averages over the ensemble of paths have a sampling error of order $1/\sqrt{N_s}$, which depends on the noise term. Such errors can be reduced further [40, 61, 62], but this involves additional complexity. Reducing sampling errors requires fast algorithms to increase N_s .

The second is the step-size or discretization error, caused by the finite size of the time-step Δt . Because noise terms have fluctuations that scale as $\Delta w \sim \sqrt{\Delta t}$, these errors requires different numerical algorithms to

achieve a given convergence order than with ordinary differential equations.

Due to the differences between drift and noise, one can usefully specify the single-step error order as $[\Delta t^n, \Delta W^m]$ [39], where the first term quantifies the zero-noise limit, and the second term the noise error, scaling as $\Delta t^{m/2}$. The global error after finite time T usually scales as $[\Delta t^{n-1}, \Delta W^{m-1}]$ [63], in the small step-size limit.

There is a third type of error, which is the global error in the projection constraint. We regard this as a distinct error, depending on the detailed constraint equations.

One can also distinguish between weak and strong convergence errors, where weak convergence measures errors in the ensemble averaged probabilities $P(\mathbf{x}, t)$ and its moments, while strong convergence measures errors of a given random trajectory $\mathbf{x}(t)$ conditioned on a specific noise $\boldsymbol{\xi}(t)$.

All stochastic methods using independent trajectories have the same scaling law for sampling errors. The local discretization and global constraint errors depend on the method used, and are treated in greater detail below.

We focus on relatively low order, high performance methods, as they are often most useful in applications. The reason for this is that the total error combines discretization and sampling errors. Reducing the discretization error using high-order methods is not as useful as with ordinary differential equations, since the increased algorithmic complexity and need for small step-sizes for convergence may lead to fewer samples and increased sampling error.

The algorithms assume a common toolbox of tangential and normal projection methods, denoted as *tang*($\boldsymbol{\delta}|\mathbf{x}_0$) and *norm*(\mathbf{x}) respectively, and defined below in detail.

B. Combined Euler projection (cEP)

Holyst [21], describes a combined Euler projected method with pure diffusion. The original proposal had no drift vector, $\mathbf{a} = 0$, and was restricted to dimensions $n = 3$ and $m = 2$. Their approach uses an Ito-Euler step in time, with a combined tangential projection of the noise at the initial point, and a normal projection at the end of the step in time. Here we describe this approach more generally by including a drift term and a constant noise matrix \mathbf{B} . We note that this Ito-type algorithm requires additional corrections if the diffusion is space-dependent. Similar techniques are used in molecular dynamics [15, 34].

In the notation of Eq (2.6), the algorithm is defined for a step starting at \mathbf{x}_0 , assuming that \mathbf{a} is the drift and \mathbf{B} is the noise matrix, as:

$$\Delta \mathbf{x} = \mathcal{P}^\perp \left(\mathbf{x} + \left(\mathbf{a}^\parallel(\mathbf{x}_0) \Delta t + \mathbf{B}^\parallel(\mathbf{x}_0) \cdot \Delta \mathbf{w} \right) \right) - \mathbf{x}. \quad (4.1)$$

The projected algorithm is described in detail in the box below:

1. Evaluate a step, $\delta = \mathbf{a}(\mathbf{x}_0) \Delta t + \mathbf{B}(\mathbf{x}_0) \cdot \Delta \mathbf{w}$.
2. Tangentially project: $\delta_{\parallel} = \text{tang}(\delta | \mathbf{x}_0)$
3. Estimate an intermediate point: $\mathbf{x}' = \mathbf{x}_0 + \delta_{\parallel}$
4. Return $\mathbf{x}_1 = \text{norm}(\mathbf{x}')$

C. Tangential midpoint projection (tMP)

We next consider purely tangential projections using a midpoint projection algorithm which can be expressed symbolically as:

$$\Delta \mathbf{x} = \mathbf{a}^{\parallel}(\bar{\mathbf{x}}, \bar{t}) \Delta t + \mathbf{B}^{\parallel}(\bar{\mathbf{x}}, \bar{t}) \Delta \mathbf{w}. \quad (4.2)$$

This method is identical to a known implicit midpoint method [39], except with a tangential drift and noise. It is expected to handle stiffness in the equations better than explicit Euler-based methods [40], and does not require knowledge of the derivatives.

From previous analysis, it has a local accuracy that depends on the properties of the noise coefficient \mathbf{B}^{\parallel} . For general noise coefficients, the strong local error is of order $[\Delta t^3, \Delta W^2]$, although this can be improved if the noise is commutative.

The relevant quantity for calculating probabilities and statistics at a finite time is the weak global error at finite time, which is of order $[\Delta t^2, \Delta W^2]$ [39, 40].

Although it converges with the given accuracy in the limit of small step-size, these conditions do not guarantee that a path stays on the manifold. This can result in substantial global errors at finite step-size. We note that a Stratonovich-type midpoint algorithm evaluates derivatives at the midpoint [39]:

1. Set $m = 0$ and $\bar{\mathbf{x}}^{(0)} = \mathbf{x}_0$.
2. $\delta = [\mathbf{a}(\bar{\mathbf{x}}^{(m)}) \Delta t + \mathbf{B}(\bar{\mathbf{x}}^{(m)}) \cdot \Delta \mathbf{w}] / 2$
3. Tangentially project: $\delta_{\parallel} = \text{tang}(\delta | \bar{\mathbf{x}}^{(m)})$
4. Estimate midpoint: $\bar{\mathbf{x}}^{(m+1)} = \mathbf{x}_0 + \delta_{\parallel}$
5. If $m < \text{iters}$, $m \rightarrow m + 1$, go to (2)
6. Return $\mathbf{x}_1 = \mathbf{x}_0 + 2\delta_{\parallel}$

This method has lower local errors than the Euler method, but as is not constrained to stay on the manifold, there is an increasing constraint error with time. This problem is removed by using an additional normal projection.

D. Combined midpoint projection (cMP)

Combined tangential and normal projection leads to an algorithm for the projected stochastic differential equation which has both good accuracy and long-term constraint stability.

It can be written symbolically as:

$$\Delta \mathbf{x} = \mathcal{P}^{\perp} \left(\mathbf{x} + \mathbf{a}^{\parallel}(\bar{\mathbf{x}}, \bar{t}) \Delta t + \mathbf{B}^{\parallel}(\bar{\mathbf{x}}, \bar{t}) \Delta \mathbf{w} \right) - \mathbf{x} \quad (4.3)$$

Both the midpoint solution and the final normal projection are obtained with fixed-point iteration.

1. Set $m = 0$ and $\bar{\mathbf{x}}^{(0)} = \mathbf{x}_0$.
2. $\delta = [\mathbf{a}(\bar{\mathbf{x}}^{(m)}) \Delta t + \mathbf{B}(\bar{\mathbf{x}}^{(m)}) \cdot \Delta \mathbf{w}] / 2$
3. Tangentially project: $\delta_{\parallel} = \text{tang}(\delta | \bar{\mathbf{x}}^{(m)})$
4. Estimate midpoint: $\bar{\mathbf{x}}^{(m+1)} = \mathbf{x}_0 + \delta_{\parallel}$
5. If $m < \text{iters}$, $m \rightarrow m + 1$, go to (2)
6. Return $\mathbf{x}_1 = \text{norm}(\mathbf{x}_0 + 2\delta_{\parallel})$

This method uses a tangential projection for each midpoint iteration, together with a final normal projection to ensure that the resulting step remains on the manifold. The reason for this choice is that the stochastic departure from the manifold is significant if allowed to propagate. The final normal projection removes this additional error.

The final projection step, if convergent, can only reduce the global error, as it constrains trajectories to the manifold with even greater accuracy. We have verified this numerically with exact examples, given below. Since the constraint is satisfied through a final normal projection, one expects that the global constraint error will be very small, and in some examples it reaches the limit of roundoff errors, about 10^{-16} with IEEE digital arithmetic.

It is important to ensure that the projected path remains on the manifold, since error-propagation often may cause a long term drift off the manifold and rapid error growth. There are two parts to the calculation, which in principle would require different numbers of iterations. In the examples we use three iterations for each part. These fixed point iterations may not converge at large step-sizes, so it is essential to compare results at different step-sizes to check this.

E. Quantitative error comparisons

Although the three methods compared here are first order, they have quite different errors in practical terms. To understand this, consider a unit circular projection in the simplest case of the driven Kubo oscillator, treated below, equivalent to $\dot{z} = iz(\omega(t) + b\xi(t))$, where $z =$

$x^1 + ix^2$, and $|z| = 1$. Defining $z = \exp(i\theta)$ gives a readily soluble exact intrinsic equation with:

$$\dot{\theta} = \omega(t) + b\xi(t). \quad (4.4)$$

This has the solution that:

$$\theta(t) = \theta(0) + \int_0^t \omega(\tau) d\tau + b\Delta w(t), \quad (4.5)$$

where $\langle \Delta w^2(t) \rangle = t$. Comparing exact results $\langle O(t) \rangle$ for an observable O , with numerical results $\langle O_A(t) \rangle$ using an algorithm A gives a truncation error defined as:

$$e(\langle O_A(t) \rangle) = \langle O_A(t) \rangle - \langle O(t) \rangle. \quad (4.6)$$

For the normally projected methods, angular errors are the only significant error, but for the methods without normal projection there is an additional radial or projection error, which grows in time as well.

1. Euler projections

For Euler projected methods starting at t_0 , with $\omega_0 = \omega(t_0)$, the angular change $\Delta\theta$ for a finite step $\Delta = \omega_0\Delta t + b\Delta w$ has a projection of:

$$\Delta\theta_E = \arctan(\Delta) \approx \Delta - \frac{1}{3}\Delta^3 + O(\Delta^5). \quad (4.7)$$

Since $\langle \Delta w^4 \rangle = 3\Delta t^2$, this leads to mean-squared displacements for pure noise evolution, of

$$\langle \Delta\theta_E^2 \rangle = b^2\Delta t - 2b^4\Delta t^2 + O(\Delta t^3). \quad (4.8)$$

Starting from $\theta_0 = 0$, the global $\langle \theta_E^2 \rangle$ error in the pure diffusion limit is therefore:

$$|e(\langle \theta_E^2 \rangle)| \leq 2tb^4\Delta t. \quad (4.9)$$

This leads to first order convergence, with global errors scaling as Δt , just as in the pure drift case.

2. Midpoint projections

By comparison, the midpoint projection leads to a much smaller local error of $\Delta^3/24$

$$\Delta\theta_{MP} = 2 \arcsin(\Delta/2) \approx \Delta + \frac{1}{24}\Delta^3. \quad (4.10)$$

For pure noise, this leads to mean-squared displacements with local errors smaller by a factor of 8. However, this error estimate is only valid with a step that commences on the manifold, in this case with $|z| = 1$. The projection error can grow in time unless a second normal projection is used. Starting from $\theta_0 = 0$, the global $\langle \theta_{MP}^2 \rangle$ error with combined projections in the pure diffusion limit is therefore:

$$|e(\langle \theta_{MP}^2 \rangle)| \leq \frac{1}{4}tb^4\Delta t. \quad (4.11)$$

This explains the much lower global errors observed numerically for cMP compared to cEP in the examples below. Including drift terms gives even greater improvements, since the method has a second order convergence in the noise-free limit with $b = 0$.

3. Higher-order methods

Since the original equation was in a Stratonovich form, any higher-order method can also be used [40], provided it is designed for a Stratonovich process and includes a tangential projection in each evaluation of the derivative. Based on the numerical experiments carried out here, one should use a normal projection to prevent drift off the manifold. Related methods have been used in free-energy sampling [35].

F. Projection algorithms

We use numerical projection algorithms defined as follows, where δ is an estimated derivative step and \bar{x} is an intermediate estimate:

1. Tangential projection of δ at \bar{x} : $\delta_{\parallel} = \text{tang}(\delta|\bar{x})$

1. Obtain normal vectors \mathbf{v}_{\perp}^j at \bar{x}
2. Calculate orthonormal gradient vectors \mathbf{n}^j from \mathbf{v}_{\perp}^j
3. Return $\delta_{\parallel} = \delta - \sum_{j=1}^m \mathbf{n}^j (\delta \cdot \mathbf{n}^j)$

2. Normal projection at \bar{x} : $\mathbf{x} = \text{norm}(\bar{x})$

1. Set $m = 0$ and $\mathbf{x}^{(0)} = \bar{x}$.
2. Obtain normal vectors \mathbf{v}_{\perp}^j and \mathbf{n}^j at $\mathbf{x}^{(m)}$
3. Evaluate $M^{ij} = \mathbf{v}_{\perp}^i \cdot \mathbf{n}^j$
4. $\mathbf{x}^{(m+1)} = \mathbf{x}_{\parallel}^{(m)} - \sum_{i,j} \mathbf{n}^i [M]_{ij}^{-1} f^j(\mathbf{x}^{(m)})$
5. If $m < \text{max}$, $m \rightarrow m + 1$, go to (2)
6. Return $\mathbf{x} = \mathbf{x}^{(m+1)}$

V. NUMERICAL EXAMPLES

In this section we give numerical examples for the algorithms. Testing convergence by reducing the step-size does not always verify that the converged result is free of errors. Therefore we use exact results and

comparisons with intrinsic methods to test and verify the projection algorithms.

An alternative method for comparisons is to check against steady-state distributions. This is restricted to long-time comparisons in cases where analytic solutions exist [35]. Exact comparisons cannot be carried out in general, since intrinsic coordinates and exact results are not always known.

Our numerical comparisons use a public domain stochastic toolbox [64] to dynamically compare different curved space diffusion SDE projection methods with an intrinsic method. We consider circular, hyper-spherical, spheroidal, catenoidal and hyperboloidal surfaces, as well as a higher dimensional polynomial surface.

These examples have positive and negative curvatures which vary in space, as well as higher dimensions and non-quadratic constraints, to cover a variety of conditions. Errors were calculated by comparison either with intrinsic simulations or with a case using a very small step-size.

Details of the Stratonovich equations used for the intrinsic calculations are given in the Appendix. Errors in the reference calculations were reduced as follows:

- The sampling errors were reduced by using 10^7 trajectories, which gives sampling errors in the range $\sim 10^{-4} - 10^{-3}$ in the means, and in all cases smaller than step-size errors.
- Step-size reductions of a factor of 5 were used for comparisons if there was no exact solution. These had five times smaller errors than the tests, so these errors were negligible.
- An implicit midpoint algorithm [39] was used for intrinsic coordinates, otherwise the most accurate projected method was used for comparisons.

Step-sizes of $\Delta t = 0.1$ and smaller were used to investigate scaling, with unit diffusion. Timings of the three methods were similar, in the ratio 0.5 : 0.7 : 1 for tMP:cEP:cMP algorithms. This is because the second projection requires fixed-point iteration, so combined methods are slower than one using tangential methods only, as one would expect.

In all figures, the two solid lines, where visible, are the upper and lower $\pm\sigma$ bounds from sampling errors in the projection algorithms with 10^7 trajectories, and the error bars indicate the sampling errors in the reference simulations.

A. Kubo oscillator

The simplest example is the projection of Euclidean noise onto a circle, giving the Kubo oscillator which is widely used as a model of microscopic noise in solid-state physics [65–67]. If $\mathbf{x} = (x, y)$ and $\mathcal{P}_{\mathbf{x}}^{\parallel}$ projects onto a unit circle with $f(\mathbf{x}) = x^2 + y^2 - 1$, this can be

written as:

$$\dot{\mathbf{x}} = \mathcal{P}_{\mathbf{x}}^{\parallel}(\mathbf{a} + \boldsymbol{\xi}), \quad (5.1)$$

where \mathbf{a} is a drift term. Defining $z = x + iy$, the projected form has a complex Stratonovich equation, $\dot{z} = iz(\omega(t) + b\xi(t))$. The corresponding intrinsic form is $\dot{\theta} = \omega(t) + b\xi(t)$, where $z = \exp(i\theta)$.

This has exact solutions for all complex moments:

$$\langle [z(t)]^m \rangle = \langle [z(0)]^m \rangle e^{(im \int_0^t \omega(\tau) d\tau - m^2 b^2 t/2)}. \quad (5.2)$$

For example, if $z(0) = b = 1$ and $\omega(t) = \omega_0 t$ to give a definite case, then:

$$\langle x(t) \rangle = e^{-t/2} \cos(\omega_0 t^2/2). \quad (5.3)$$

Table (I) gives comparative errors using the different algorithms, for the case $b = 1$ and $\omega_0 = 2.5$. A comparative graph of mean values is given in Fig(1).

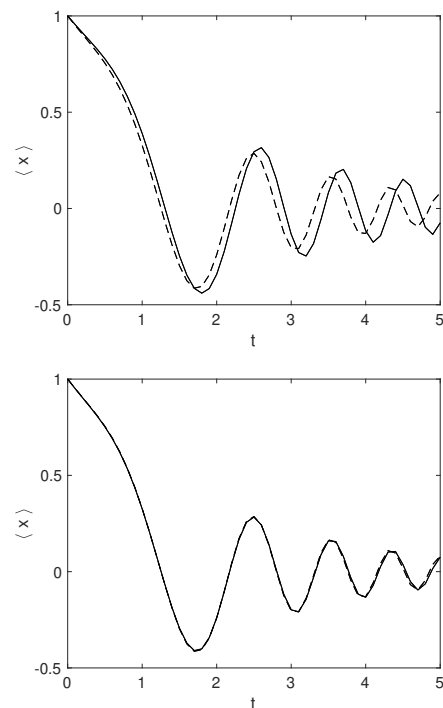


Figure 1. Comparing projection algorithms for the Kubo oscillator case with a step-size of 0.05. The solid lines are simulations, dashed lines are the exact results. Top: combined Euler projection method (cEP). Bottom, combined midpoint projection method (cMP).

For a step-size $\Delta t = 0.05$, the combined midpoint method has ~ 10 times lower maximum errors in $\langle x \rangle$ than the Euler method, and over 10^{12} times lower maximum projection errors than the tangential method. The quadratic error reduction in the combined midpoint method occurs because the step-size error is dominated by the drift term. In this limit, the midpoint method has second-order global error convergence. Sampling errors are of order 2×10^{-4} .

Function	Step	cEP	tMP	cMP
$\langle x \rangle$	0.1	0.38	0.11	0.11
	0.05	0.19	2×10^{-2}	2×10^{-2}
$\langle f \rangle$	0.1	3.7×10^{-5}	0.3	1.2×10^{-5}
	0.05	1.8×10^{-7}	0.03	6×10^{-16}

Table I. Comparison of maximum error of combined Euler projection (cEP), tangential midpoint projection (tMP), and combined midpoint projections (cMP) for Kubo oscillator, using time-steps of 0.1 and 0.05, with 10^7 parallel trajectories, $t_{max} = 5$ and $\omega_0 = 2.5$.

B. Catenoid

The catenoid is an hyperbola rotated around an axis, and is a surface of zero curvature. Despite the fact that the geometry is non-planar, it has linear growth in diffusion distance with time, just as a planar surface has. This is a minimal surface, defined by the constraint that [68]:

$$x^2 + y^2 - \sinh^2 z = 1. \quad (5.4)$$

A convenient set of intrinsic coordinates is [68]:

$$\begin{aligned} x &= \cosh v \cos \theta, \\ y &= \cosh v \sin \theta, \\ z &= v, \end{aligned} \quad (5.5)$$

For unit diffusion, so $D = B = I$, the exact solution for the average diffusion distance is [69]:

$$\langle |\mathbf{x} - \mathbf{x}_0|^2 \rangle = 2t. \quad (5.6)$$

A maximum error comparison is shown in Table (II), using time-steps of 0.1 and 0.05, with a duration of $t_{max} = 5$ and 10^7 parallel trajectories. Sampling errors in distance are of order 3×10^{-3} .

Function	Δt	cEP	tMP	cMP
$\langle R^2 \rangle$	0.1	0.45	7.8×10^{-2}	5.7×10^{-2}
	0.05	0.24	4.4×10^{-2}	3.3×10^{-2}
$\langle f \rangle$	0.1	7.6×10^{-8}	7.3×10^{-2}	3.2×10^{-13}
	0.05	2.2×10^{-10}	4×10^{-2}	1.6×10^{-15}

Table II. Comparison of maximum error of combined Euler projection (cEP), tangential midpoint projection (tMP), and combined midpoint projection (cMP) methods for diffusion on a catenoid.

For a step-size of 0.05, the advantage of the cMP method is a factor of more than 8 reduction in mean square distance error compared to combined Euler projection, and more than 10^{12} reduction in constraint error compared to tangential midpoint projection.

C. Spheroid

An ellipsoid is defined by the constraint equation [70]

$$x^2/a^2 + y^2/b^2 + z^2/c^2 - 1 = 0. \quad (5.7)$$

Setting $a = b = 1$ gives a spheroid, which is a distortion of the unit sphere along one axis. The metric tensor on the spheroid simplifies greatly compared to the general ellipsoid, and we restrict ourselves to this shape. In order to test the projection algorithms, we compare the results of the projected SDE to a direct simulation of diffusion on the spheroid using the intrinsic coordinates of:

$$\begin{aligned} x &= \sin \theta \cos \phi, \\ y &= \sin \theta \sin \phi, \\ z &= c \cos \theta, \end{aligned} \quad (5.8)$$

with $0 \leq \theta \leq \pi$ and $0 \leq \phi < 2\pi$. The equations used for this are derived in the Appendix, and are:

$$\begin{aligned} \dot{\theta} &= -\frac{\cot \theta}{(c^2 - 1) \cos 2\theta - (1 + c^2)} + \frac{\xi^\theta}{\sqrt{\cos^2 \theta + c^2 \sin^2 \theta}} \\ \dot{\phi} &= \frac{\xi^\phi}{\sin \theta}. \end{aligned} \quad (5.9)$$

The initial point in the simulations was at $\theta = \phi = 1$, which is a large distance from any singularity. This was allowed to diffuse following the spheroidal diffusion equations for a time-interval of $t_{max} = 1$. The results are shown in Figs (2, 3, 4 & 5), where $c = 0.25$ was chosen. The measure of distance used for these figures is the great circle distance, defined as

$$\Theta(\mathbf{x}, \mathbf{y}) = \cos^{-1}(\mathbf{x}^T G \mathbf{y}). \quad (5.10)$$

The results given in Table (III) show that the cMP algorithm gives excellent agreement between the intrinsic and the projected SDE results.

Function	Δt	cEP	tMP	cMP
$\langle \Theta(\mathbf{x}, \mathbf{x}_0) \rangle$	0.02	0.097	0.1	1.5×10^{-2}
	0.01	6.4×10^{-2}	3.7×10^{-2}	4.2×10^{-3}
$\langle f \rangle$	0.02	1.08×10^{-4}	0.4	1.3×10^{-5}
	0.01	9.9×10^{-6}	0.19	6×10^{-7}

Table III. Comparison of maximum error of combined Euler projection (cEP), tangential midpoint projection (tMP), and combined midpoint projection (cMP) methods for diffusion on an spheroidal surface, using time-steps of 0.02 and 0.01 with 10^7 parallel trajectories. Distance sampling errors are at most 2.4×10^{-4} .

Owing to the strong curvature of spheroid, we use smaller step-sizes than the previous examples. For step-sizes of 0.01, the computational advantage of the cMP method in this case is 16 times reduction in distance

error compared to cEP, and 1.6×10^5 times reduction in constraint error compared to tMP.

For all figures, the two solid lines are the upper and lower $\pm\sigma$ bounds from sampling errors in the differences, and a step size of 0.01 is used.

1. Combined Euler projection algorithm (cEP)

Because of the final projection employed, this algorithm shows a typical behavior of relatively high distance errors, but good ability to maintain the trajectory on the manifold.

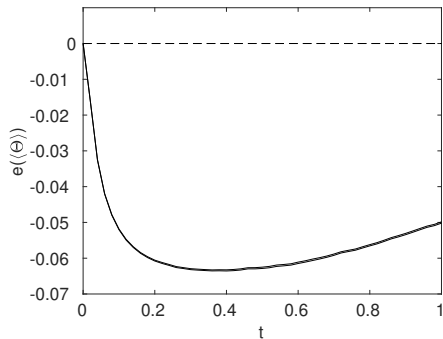


Figure 2. cEP mean great circle distance error, $e(\langle\Theta\rangle)$ for diffusion on a spheroid.

2. Tangential midpoint projection algorithm (tMP)

Because of the midpoint tangential projection employed, this algorithm shows improved convergence with step-size, but is unable maintain the trajectory on the manifold.

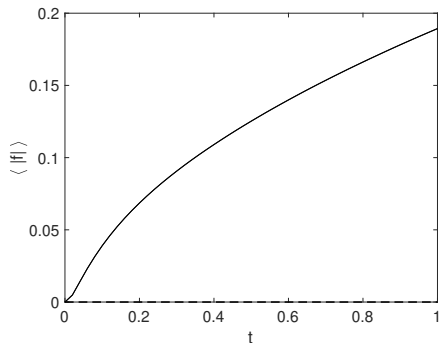


Figure 3. (Constraint error of the tMP algorithm for diffusion on a spheroid.

3. Combined midpoint projection algorithm (cMP)

Using the combined tangential projection employed, this algorithm shows greatly improved convergence with

step-size, and is able to maintain the trajectory on the manifold.

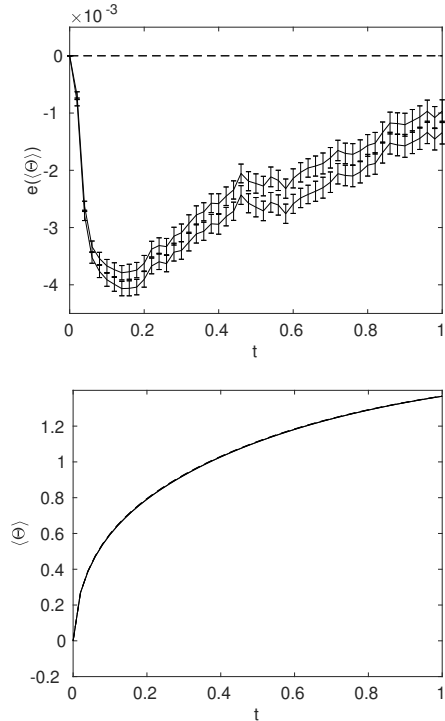


Figure 4. (Top) cMP mean great circle distance error, $e(\langle\Theta\rangle)$. The two solid lines are the upper and lower sampling error bars ($\pm\sigma$) of the projected simulation, and the error-bars indicate the sampling errors of the intrinsic method, both with 10^7 trajectories. (Bottom) Comparison of the cMP algorithm mean great-circle distance (solid lines) to a simulation of diffusion on the spheroid in intrinsic coordinates (dotted lines).

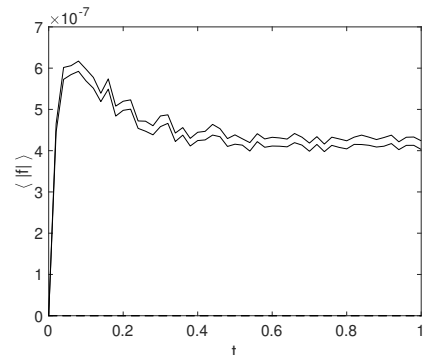


Figure 5. Constraint error of the cMP algorithm simulation of diffusion on the spheroid. The two solid lines are the upper and lower sampling error bars ($\pm\sigma$) of the projected simulation.

D. Hyperboloid

The next example we consider is that of the one-sheeted hyperboloid, defined by the constraint equation [70]

$$x^2/a^2 + y^2/b^2 - z^2/c^2 - 1 = 0. \quad (5.11)$$

and the intrinsic coordinates:

$$\begin{aligned} x &= \cosh v \cos \theta, \\ y &= \cosh v \sin \theta, \\ z &= c \sinh v. \end{aligned} \quad (5.12)$$

We choose $a = b = 1$ and $c = 0.25$ to simplify the metric tensor, which is required to obtain the intrinsic SDEs for diffusion on this manifold. Details are given in the Appendix.

The corresponding intrinsic equations are

$$\begin{aligned} \dot{v} &= \frac{\tanh v}{c^2 - 1 + (c^2 + 1) \cosh 2v} + \frac{\xi^v}{\sqrt{\sinh^2 v + c^2 \cosh^2 v}}, \\ \dot{\theta} &= \frac{\xi^\theta}{\cosh v}. \end{aligned} \quad (5.13)$$

Applying the three different projection algorithms for SDEs yields Figs (6, 7, 9 & 8), where we use the Euclidean distance [71] measure,

$$R(\mathbf{x}, \mathbf{y}) = \|\mathbf{x} - \mathbf{y}\|. \quad (5.14)$$

The initial point in the simulations was at $\theta = v = 0$. This was allowed to diffuse following the spheroidal diffusion equations for a time-interval of $t_{max} = 1$. Similar to the spheroid, there is almost exact agreement between the intrinsic and hybrid midpoint projected SDE algorithms, with poor convergence in the other two cases.

Function	Δt	cEP	tMP	cMP
$\langle \mathbf{x} - \mathbf{x}_0 ^2 \rangle$	0.02	0.14	1.4×10^{-2}	1.4×10^{-2}
	0.01	9×10^{-2}	1.9×10^{-3}	4.7×10^{-3}
$\langle f \rangle$	0.02	2.9×10^{-4}	0.29	3×10^{-4}
	0.01	1.8×10^{-5}	0.15	2.4×10^{-6}

Table IV. Comparison of maximum error of combined Euler projection (cEP), tangential midpoint projection (tMP), and combined midpoint projection (cMP) methods for diffusion on a hyperboloidal surface, using time-steps of 0.02 and 0.01 with 10^7 parallel trajectories. Distance sampling errors are at most 6.9×10^{-4} .

Because of the relatively strong curvature, we use step-sizes of 0.02 and 0.01. The above table shows that the computational advantage of the cMP method. At a step-size of .01, there is about 16 times reduction in mean squared distance error compared to cEP, and a 10^4 times reduction in constraint error compared to the tMP algorithm.

1. Combined Euler projection algorithm (cEP)

As in the spheroidal case, this algorithm shows relatively poor convergence with step-size, but is able to maintain the trajectory on the manifold, due to the use of a normal projection.

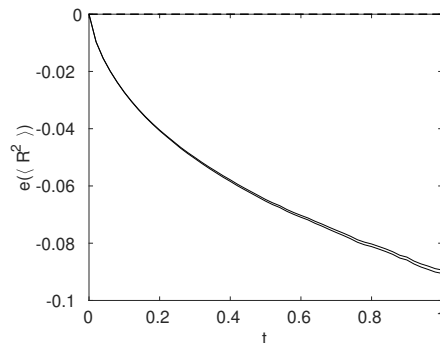


Figure 6. (Top): cEP mean square distance error, $e(\langle R^2 \rangle)$ is plotted. (Bottom) Constraint error of the cEP method for diffusion on a hyperboloid.

2. Tangential midpoint projection algorithm (tMP)

This algorithm shows improved convergence with step-size, but is less able to maintain the trajectory on the manifold, with very large constraint errors.

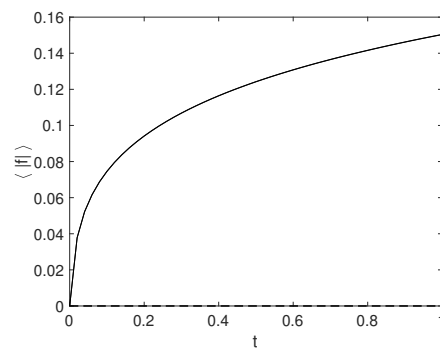


Figure 7. (Top): tMP mean square distance error, $e(\langle R^2 \rangle)$ is plotted. (Bottom) Constraint error of the tMP algorithm for diffusion on the hyperboloid.

3. Combined midpoint projection algorithm (cMP)

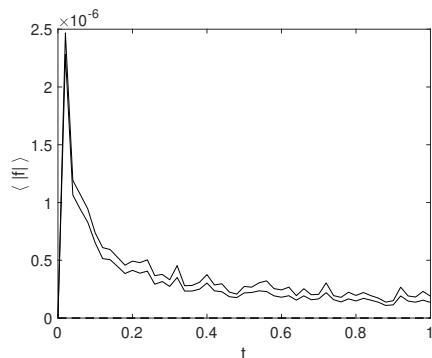


Figure 8. Constraint error of the cMP algorithm simulation of diffusion on the hyperboloid.

This algorithm repeats the trend in the spheroidal case, with both improved convergence with step-size, and much greater ability to maintain the trajectory on the manifold.

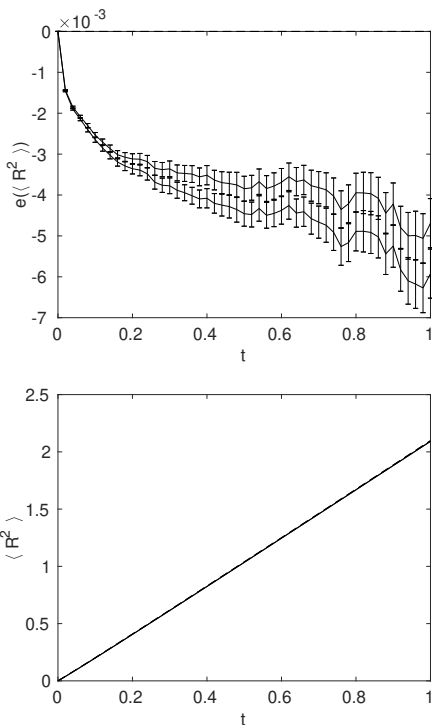


Figure 9. (Top) cMP mean square distance error is plotted. (Bottom) Comparison of the cMP algorithm mean square Euclidean distance (solid lines) to a simulation of diffusion on the hyperboloid in intrinsic coordinates (dotted lines).

We note the almost linear growth in the mean square diffusion distance. This is caused by our starting point at $z = c \sinh v = 0$. Apart from a scaling of the z -distance, in the small- z regime the hyperboloidal geometry is similar to a catenoid with $z = v$, which has an

exactly linear growth.

E. Polynomial surface

A more general N -th order polynomial manifold in n dimensions was investigated, with a constraint of:

$$\sum_{j=1}^n [x^j]^N = 1. \quad (5.15)$$

This example is applicable to arbitrary dimensions. In the three-dimensional case, for powers $N \gg 2$, this gives a nearly cubic surface with rounded edges, corresponding to a rapidly varying curvature, as in some biological cell walls. To give a model of transport, we include an axial force as a drift term.

The projected SDE can be written as in Eq (3.39) as:

$$\dot{\mathbf{x}} = \mathcal{P}_{\mathbf{x}}^{\parallel}(\mathbf{a} + \boldsymbol{\xi}), \quad (5.16)$$

where $\mathbf{a} = [0, 0, 2z]$, thus modeling an outward axial force in the z direction.

Here we use a quartic constraint: $N = 4$, to give an inhomogeneous, non-spherical surface. As there are neither exact solutions nor intrinsic variables, the reference solutions were obtained using the cMP algorithm with much smaller step-sizes. An error comparison is shown in Table (V).

Function	Δt	cEP	tMP	cMP
$\langle R^2 \rangle$	0.1	0.14	0.12	1.7×10^{-2}
	0.05	0.08	0.07	9.9×10^{-3}
$\langle f \rangle$	0.1	2.8×10^{-4}	0.3	1.7×10^{-5}
	0.05	1.3×10^{-5}	0.16	4×10^{-9}

Table V. Comparison of maximum error of combined Euler projection (cEP), tangential midpoint projection (tMP), and combined midpoint projection (cMP) methods for diffusion on a 3-dimensional, fourth-order polynomial surface, using time-steps of 0.1 and 0.05, with 10^7 parallel trajectories, and a duration of $t_{max} = 5$. Distance sampling errors are less than 5×10^{-4} .

As in the earlier examples, the distance errors with the cMP algorithm are smaller by nearly an order of magnitude than with the other algorithms.

F. Hypersphere

We finally consider much higher dimensions, using an n -dimensional hyper-spherical manifold with $|\mathbf{x}|^2 = 1$ and isotropic unit diffusion in the original Euclidean space. If $\mathcal{P}_{\mathbf{x}}^{\parallel}$ is a hyperspherical surface projection, the projected SDE can be written as in Eq (3.39). This has exact solutions for the expected diffusion distance, $R = |\mathbf{x} - \mathbf{x}_0|$ [69]:

$$\langle R^2 \rangle = 2 \left(1 - \exp \left(-\frac{n-1}{2} t \right) \right). \quad (5.17)$$

Numerical results for errors in ten space dimensions is shown in Table (VI).

Function	Δt	cEP	tMP	cMP
$\langle R^2 \rangle$	0.1	0.29	0.27	2.1×10^{-2}
	0.05	0.17	0.11	9.8×10^{-3}
$\langle f \rangle$	0.1	1.0×10^{-5}	0.3	7.8×10^{-11}
	0.05	2.8×10^{-7}	0.11	2.3×10^{-16}

Table VI. Comparison of maximum error of combined Euler projection (cEP), tangential midpoint projection (tMP), and combined midpoint projection (cMP) methods for diffusion on a 10-dimensional hypersphere, using time-steps of 0.1 and 0.05.

The computational advantage of the cMP method increases in higher dimensions. In $n = 10$ dimensions, for a step-size of 0.05, the improvement for cMP is a factor of 17 in mean square distance error reductions compared to cEP, and over 10^9 in constraint error reductions compared to either alternative. In these tests, the duration is $t_{max} = 5$, with 10^7 parallel trajectories. Sampling errors are of order 2×10^{-4} . Graphical comparisons are shown in Fig (10).

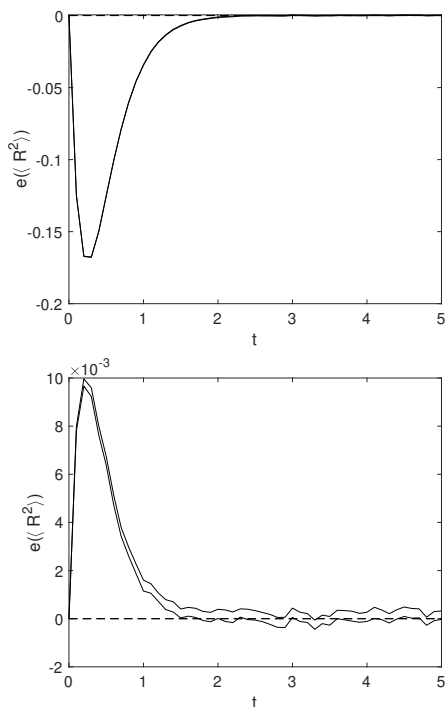


Figure 10. Comparing errors for the 10-sphere diffusion case with a step-size of 0.05. The solid lines are upper and lower sampling error bars of the simulations. Top: combined Euler projection method (cEP). Bottom: combined midpoint projection method (cMP).

The ratio of errors obtained in the Kubo oscillator case, with an 8:1 improvement in error for the midpoint versus the Euler method, is even greater in these higher-dimensional results. After correcting for the increased diffusion in ten dimensions, these errors are within the global error bounds of Eqs (4.9) and (4.11).

VI. SUMMARY OF RESULTS

In summary, we have shown how projected SDEs are derived using adiabatic elimination with a constraint potential, and that the projected equation is a Stratonovich type. We have obtained a combined midpoint projection algorithm for projecting a stochastic equation onto a general manifold, and compared it to earlier proposals, using numerical studies on multiple surfaces with positive and negative curvature, having different dimensions and constraint equations.

The hybrid midpoint algorithm gives a distinctly improved error performance compared to both the earlier algorithms used for comparison. The improvement is due to a combination of tangential and normal projections, together with a more accurate midpoint algorithm. The combined Euler projection method cannot accurately track the changes in the projected drift and diffusion terms during a step, as it relies on an initial estimate of the diffusion, which changes in space due to the projection. The midpoint projection method has an improved treatment of diffusion, but is unable to control global error growth when trajectories move off the manifold.

Adaptive step-size [72] or higher order methods are possible [40, 73, 74]. These are also suggested for projected equations [35, 75], and provide other alternatives.

Yet there are multiple factors [61, 62] causing numerical errors. The combined midpoint projected method combines good discretization error performance with low complexity, straightforward parallel implementation, and reasonable speed. This is a great advantage when it is important to reduce both sampling error and discretization errors.

In summary, the combined midpoint projection method, which allows for changes in the diffusion matrix and maintains the constraint, has much greater accuracy than either method used for comparisons. This comparative performance is proved as an error bound for the simple case of the Kubo oscillator, and demonstrated numerically in more complex examples. This implies that, for identical error performance, the cMP method can use larger steps, and is up to an order of magnitude more efficient than the cEP algorithm.

ACKNOWLEDGEMENTS

This work was funded through an Australian Research Council Discovery Project Grant DP190101480, and a grant from NTT Research. PDD acknowledges

the hospitality of the Aspen Center for Physics, supported by NSF grant PHY-1607611, the Institute for Atomic and Molecular Physics (ITAMP) at Harvard University, supported by the NSF, and the Joint Institute for Laboratory Astrophysics at University of Colorado.

APPENDIX: SPHEROIDAL AND HYPERBOLOIDAL INTRINSIC STOCHASTIC EQUATIONS

Spheroidal diffusion

As an example in the main text, a 2-spheroid may be embedded in \mathbb{R}^3 by the constraint equation [70]

$$x^2 + y^2 + z^2/c^2 = 1. \quad (6.1)$$

Applying Eq. (3.27), one obtains the inverse metric tensor

$$(g^{\mu\nu}) = \text{diag} \left(\frac{1}{\cos^2 \theta + c^2 \sin^2 \theta}, \frac{1}{\sin^2 \theta} \right), \quad (6.2)$$

where the intrinsic coordinates θ and ϕ are related to the extrinsic coordinates as [70]

$$\begin{aligned} x &= \sin \theta \cos \phi, \\ y &= \sin \theta \sin \phi, \\ z &= c \cos \theta, \end{aligned} \quad (6.3)$$

with $0 \leq \theta \leq \pi$ and $0 \leq \phi < 2\pi$.

From the diffusion tensor in Eq. (6.2) and the relation in Eq. (3.32), one can find the self adjoint drift as,

$$\alpha_a^\theta = \frac{\cos \theta \left[\sin \theta (c^2 - 1) + \frac{1}{2 \sin \theta} \right]}{(\cos^2 \theta + c^2 \sin^2 \theta)^2}, \quad (6.4)$$

$$\alpha_a^\phi = 0. \quad (6.5)$$

This can be converted to a Stratonovich drift by making use of Eq. (3.33):

$$\alpha^\theta = \frac{\cot \theta}{2 (\cos^2 \theta + c^2 \sin^2 \theta)}, \quad (6.6)$$

$$\alpha^\phi = 0. \quad (6.7)$$

This in turn can be utilized to find the intrinsic Stratonovich SDE as:

$$\begin{aligned} \dot{\theta} &= -\frac{\cot \theta}{(c^2 - 1) \cos 2\theta - (1 + c^2)} + \frac{\xi^\theta}{\sqrt{\cos^2 \theta + c^2 \sin^2 \theta}} \\ \dot{\phi} &= \frac{\xi^\phi}{\sin \theta}. \end{aligned} \quad (6.8)$$

Hyperboloidal diffusion

As another example used in the main text, the one-sheeted hyperboloid is defined by the constraint [68, 70]

$$x^2 + y^2 - z^2/c^2 = 1. \quad (6.9)$$

A convenient set of intrinsic coordinates is given by [70]

$$\begin{aligned} x &= \cosh v \cos \theta, \\ y &= \cosh v \sin \theta, \\ z &= c \sinh v, \end{aligned} \quad (6.10)$$

where $-\infty < v < \infty$ and $0 \leq \theta < \pi$. This yields the inverse metric

$$(g^{\mu\nu}) = \text{diag} \left(\frac{1}{\sinh^2 v + c^2 \cosh^2 v}, \frac{1}{\cosh^2 v} \right), \quad (6.11)$$

and making use of the above equation, (3.32) and (3.33) one obtains an intrinsic Stratonovich SDE:

$$\begin{aligned} \dot{v} &= \frac{\tanh v}{c^2 - 1 + (c^2 + 1) \cosh 2v} + \frac{\xi^v}{\sqrt{\sinh^2 v + c^2 \cosh^2 v}}, \\ \dot{\theta} &= \frac{\xi^\theta}{\cosh v}. \end{aligned} \quad (6.12)$$

-
- [1] R. J. Cherry, *Biochimica et Biophysica Acta (BBA)-Reviews on Biomembranes* **559**, 289 (1979).
[2] D. R. Brillinger, *Journal of Theoretical Probability* **10**, 429 (1997).
[3] L. C.-L. Lin and F. L. Brown, *Biophysical journal* **86**, 764 (2004).
[4] I. F. Sbalzarini, A. Hayer, A. Helenius, and P. Koumoutsakos, *Biophysical journal* **90**, 878 (2006).
[5] I. L. Novak, F. Gao, Y.-S. Choi, D. Resasco, J. C. Schaff, and B. M. Slepchenko, *Journal of computational physics* **226**, 1271 (2007).
[6] A. M. Gusak, T. Zaporozhets, Y. O. Lyashenko, S. Kornienko, M. Pasichnyy, and A. Shirinyan, *Diffusion-controlled Solid State Reactions: In Alloys, Thin Films and Nanosystems* (John Wiley & Sons, 2010).
[7] C. J. S. Klaus, K. Raghunathan, E. DiBenedetto, and A. K. Kenworthy, *Molecular biology of the cell* **27**, 3937 (2016).
[8] J. Adler, I.-M. Sintorn, R. Strand, and I. Parmryd, *Communications biology* **2**, 1 (2019).
[9] P. Castro-Villarreal and F. J. Sevilla, *Physical Review E* **97**, 052605 (2018).
[10] M. Smerlak, *New Journal of Physics* **14**, 023019 (2012).
[11] I. Kosztin, B. Faber, and K. Schulten, *American Journal of Physics* **64**, 633 (1996).
[12] D. C. Mattis and M. L. Glasser, *Reviews of Modern Physics* **70**, 979 (1998).

- [13] W. Zhou, L. Zhang, J. Hong, and S. Song, *BIT Numerical Mathematics* **56**, 1497 (2016).
- [14] S. Albeverio and S.-M. Fei, *Journal of Physics A: Mathematical and General* **28**, 6363 (1995).
- [15] G. Ciccotti, T. Lelièvre, and E. Vanden-Eijnden, *Communications on Pure and Applied Mathematics: A Journal Issued by the Courant Institute of Mathematical Sciences* **61**, 371 (2008).
- [16] M. Schonlau, W. J. Welch, and D. R. Jones, *Lecture Notes-Monograph Series*, 11 (1998).
- [17] A. J. Lee, W.-c. Lin, and C.-s. Wang, *Journal of Systems and Software* **79**, 79 (2006).
- [18] T. Meng and W. He, *IEEE Transactions on Industrial Electronics* **65**, 664 (2017).
- [19] J. Carius, R. Ranftl, F. Farshidian, and M. Hutter, *The International Journal of Robotics Research*, 02783649211047890 (2021).
- [20] M. Stilman, *IEEE Transactions on Robotics* **26**, 576 (2010).
- [21] R. Hołyst, D. Plewczyński, A. Aksimentiev, and K. Burdzy, *Physical Review E* **60**, 302 (1999).
- [22] L. Chierchia and G. Gallavotti, in *Annales de l'IHP Physique théorique*, Vol. 60 (1994) pp. 1–144.
- [23] K. Ngai and R. Rendell, *Journal of non-crystalline solids* **131**, 233 (1991).
- [24] J. Thomson and G. Benford, *Physical Review Letters* **28**, 590 (1972).
- [25] R. R. Joseph, L. E. C. Rosales-Zárate, and P. D. Drummond, *J. Phys. A* **51**, 245302 (2018).
- [26] R. R. Joseph, L. E. C. Rosales-Zárate, and P. D. Drummond, *Phys. Rev. A* **98**, 013638 (2018).
- [27] C. Beenakker, *Annu. Rev. Condens. Matter Phys.* **4**, 113 (2013).
- [28] F. Wilczek, *Nature Physics* **5**, 614 (2009).
- [29] R. Graham, *Physical Review Letters* **38**, 51 (1977).
- [30] R. Graham, *Zeitschrift für Physik B* **26**, 397 (1977).
- [31] R. R. Joseph, L. E. Rosales-Zárate, and P. D. Drummond, arXiv preprint arXiv:2104.11925 (2021).
- [32] C. W. Gardiner, *Handbook of Stochastic Methods*, 2nd ed. (Springer-Verlag, Berlin, 1985) p. 442.
- [33] H. C. Andersen, *Journal of computational Physics* **52**, 24 (1983).
- [34] T. Lelièvre, M. Rousset, and G. Stoltz, *Free energy computations: a mathematical perspective* (Imperial College Press, 2010).
- [35] A. Laurent and G. Vilmart, *Foundations of Computational Mathematics*, 1 (2021).
- [36] H. Whitney, *Annals of Mathematics*, 645 (1936).
- [37] H. Whitney, *Annals of Mathematics*, 220 (1944).
- [38] J. Nash, *Annals of mathematics*, 20 (1956).
- [39] P. D. Drummond and I. K. Mortimer, *J. Comput. Phys.* **93**, 144 (1991).
- [40] P. E. Kloeden and E. Platen, *Numerical Solution of Stochastic Differential Equations* (Springer-Verlag, Berlin, 1992).
- [41] G. N. Milstein, *Numerical integration of stochastic differential equations*, Vol. 313 (Springer Science & Business Media, 1994).
- [42] M. Bertalmio, L.-T. Cheng, S. Osher, and G. Sapiro, *Journal of Computational Physics* **174**, 759 (2001).
- [43] N. S. Hawley, *Annals of Mathematics*, 637 (1950).
- [44] H. Poincaré, *J. Math. Pures Appl.* **4**, 167 (1885).
- [45] H. Hopf, *Mathematische Annalen* **96**, 225 (1927).
- [46] M. Émery, in *Séminaire de Probabilités XXIV 1988/89* (Springer, 1990) pp. 407–441.
- [47] D. A. Calhoun and C. Helzel, *SIAM Journal on Scientific Computing* **31**, 4066 (2010).
- [48] J. Armstrong, D. Brigo, and E. Rossi Ferrucci, *Proceedings of the London Mathematical Society* **119**, 176 (2019).
- [49] R. L. Stratonovich, *SIAM J. Control* **4**, 362 (1966).
- [50] C. Gardiner, *Physical Review A* **29**, 2814 (1984).
- [51] T. Frankel, *The geometry of physics: an introduction* (Cambridge university press, 2011).
- [52] P. C. Schuster and R. Jaffe, *Annals of Physics* **307**, 132 (2003).
- [53] L. N. Trefethen and D. Bau III, *Numerical linear algebra*, Vol. 50 (Siam, 1997).
- [54] X. Chen and W. Ye, *Electronic Journal of Probability* **26**, 1 (2021).
- [55] C. Pozrikidis and D. Jankowski, *Introduction to theoretical and computational fluid dynamics*, Vol. 675 (Oxford university press New York, 1997).
- [56] H. Risken, *The Fokker-Planck Equation*, 2nd ed. (Springer-Verlag, Berlin, 1996).
- [57] L. Arnold, *Stochastic differential equations: theory and applications*, reprint ed. (Folens Publishers, 1992) p. 228.
- [58] S. Gustafsson and B. Halle, *The Journal of Chemical Physics* **106**, 1880 (1997).
- [59] Y. Yang and B. Li, *The Journal of chemical physics* **151**, 164901 (2019).
- [60] P.-O. Löwdin, *The Journal of Chemical Physics* **18**, 365 (1950).
- [61] B. Opanchuk, S. Kiesewetter, and P. D. Drummond, *SIAM Journal on Scientific Computing* **38**, A3857 (2016).
- [62] S. Kiesewetter and P. D. Drummond, *Computer Physics Communications* **212**, 25 (2017).
- [63] G. Milstein, *Theory of Probability & Its Applications* **19**, 557 (1975).
- [64] S. Kiesewetter, R. Polkinghorne, B. Opanchuk, and P. D. Drummond, *SoftwareX* **5**, 12 (2016).
- [65] P. W. Anderson, *Journal of the Physical Society of Japan* **9**, 316 (1954).
- [66] R. Kubo, *Journal of the Physical Society of Japan* **9**, 935 (1954).
- [67] J. R. Chaudhuri and S. Chattopadhyay, *Chemical Physics Letters* **480**, 140 (2009).
- [68] M. Berger and B. Gostiaux, *Differential Geometry: Manifolds, Curves, and Surfaces: Manifolds, Curves, and Surfaces*, Vol. 115 (Springer Science & Business Media, 2012).
- [69] P. Castro-Villarreal, *Journal of Statistical Mechanics: Theory and Experiment* **2014**, P05017 (2014).
- [70] A. Gray, E. Abbena, and S. Salamon, *Modern differential geometry of curves and surfaces with Mathematica®* (Chapman and Hall/CRC, 2017).
- [71] H. Cartan, “Differential calculus. hermann,” (1971).
- [72] H. Lamba, *Journal of computational and applied mathematics* **161**, 417 (2003).
- [73] K. Burrage and P. M. Burrage, *Applied Numerical Mathematics* **22**, 81 (1996).
- [74] K. Burrage and P. M. Burrage, *SIAM Journal on Numerical Analysis* **38**, 1626 (2000).
- [75] A. Abdulle, G. Vilmart, and K. C. Zygalakis, *SIAM Journal on Numerical Analysis* **52**, 1600 (2014).